STATISTICS, OPTIMIZATION AND INFORMATION COMPUTING
Stat., Optim. Inf. Comput., Vol. **13**, January 2025, pp 138–157.
Published online in International Academic Press (www.IAPress.org)

Magnetic Resonance Image Restoration by Utilizing Fractional-Order Total Variation and Recursive Filtering

Nana Wei [1], Wei Xue [1,3,*], Xiaolei Gu [2,3], Xuan Qi [2,3]

[1]*School of Computer Science and Technology, Anhui University of Technology, Maanshan 243032, China*
[2]*Department of Radiology, Maanshan People's Hospital, Maanshan 243099, China*
[3]*Maanshan Key Laboratory for Medical Image Modeling and Intelligent Analysis, Maanshan 243099, China*

Abstract Total variation-based methods are effective for magnetic resonance image restoration. To eliminate impulse noise, the ℓ_0-norm total variation model is a proven approach. However, traditional total variation image restoration often results in staircase artifacts, especially at high noise levels. In this paper, we propose an innovative magnetic resonance image restoration model that integrates fractional-order regularization and filtering techniques. Specifically, the first term uses the ℓ_0-norm as the data fidelity term to effectively remove impulse noise. The second term introduces a fractional-order total variation regularizer, which preserves structural information while reducing staircase artifacts during deblurring. Due to its limitations in texture detail recovery, we employ recursive filtering for high-quality edge-preserving filtering. Finally, we solve the optimization model using the alternating direction method of multipliers. Experimental results demonstrate the effectiveness of our method in restoring magnetic resonance images.

Keywords Magnetic resonance image restoration, ℓ_0-norm, fractional-order total variation, recursive filtering

AMS 2010 subject classifications 68U10, 65K15

DOI: 10.19139/soic-2310-5070-2291

1. Introduction

Magnetic Resonance (MR) imaging is a powerful tool in the field of medical imaging, used for diagnosing and monitoring various diseases. However, the quality of MR images can often be compromised by the presence of impulse noise, which appears as sparsely occurring white and black pixels. This type of noise can significantly degrade image quality, making it difficult for medical professionals to interpret the images accurately. Impulse noise in MR images can arise from several factors, including hardware faults, transmission errors, and other interferences. The challenge of image restoration lies in developing effective methods to remove this noise while preserving important details and edges in the images.

In the quest to eliminate impulse noise from MR images, a spectrum of methodologies has been meticulously investigated. Among these, regularization techniques and filtering strategies stand out as particularly effective. A cornerstone in the realm of medical image restoration is the total vriation (TV) model, which has demonstrated remarkable efficacy in denoising, deblurring, segmentation, and superresolution tasks. However, the TV model encounters limitations when confronted with noise in piecewise affine regions, often manifesting as undesirable staircase artifacts. To address this limitation, a variety of regularization techniques have been introduced. Such as, the High-Order TV method [3], Non-Convex High-Order TV [4], Fractional-Order TV (FOTV). [5] and [6] are among the notable advancements, their numerical experiments showed that their methods alleviated the staircase

*Correspondence to: Wei Xue (Email: xuewei@ahut.edu.cn).

ISSN 2310-5070 (online) ISSN 2311-004X (print)

effect effectively. Additionally, [2] introduced the Overlapping Group Sparse Fractional-Order TV (OGSTV), which has garnered attention for its refined approach. Besides, [10] proposed an enhanced ℓ_1-NCFOTV method, which promises to elevate the restoration precision of images afflicted by impulse noise and to diminish the staircase effect.

In the realm of filtering, the median filter (MF) and adaptive median filter (AMF) [22] have long been established as fundamental tools in denoising efforts. Despite their widespread use, these filters struggle with high noise intensities, leading to the development of more advanced techniques such as recursive filtering, recursive mean filtering, a non-local adaptive mean filter (NAMF) [8] and improved median filter [9]. Additionally, recursive filtering demonstrates effective performance in restoring edges. To effectively eliminate impulse noise, the ℓ_2-norm [1] is sensitive to outliers and can easily result in unsatisfactory image restoration. It is commonly used for images degraded by additive Gaussian noise. There has been a growing interest in using an ℓ_1-fidelity term instead of the ℓ_2-fidelity term for image restoration, as seen in many studies such as [11, 12]. Numerical evidence clearly indicates that the proposed method has made substantial advancements in its capacity for restoration. While the ℓ_1-norm has been recognized for its benefits in sparse signal processing and image restoration, it has been noted that it might excessively penalize the resulting solution in the context of impulse noise elimination, as highlighted by [7].

To circumvent this issue, a method for removing impulse noise using ℓ_0 total variation (ℓ_0-TV) was proposed in [13]. This method employs the ℓ_0-norm for the data fidelity and uses the proximal alternating direction method of multipliers (ADMM) for image restoration. The empirical evidence show better performance than ℓ_1-norm based methods. Consequently, this indicates that ℓ_0-norm is suitable for the restoration of images distorted by impulse noise. The image restoration of the optimization problem can be depicted as

$$\min_u \|o \odot (Hu - b)\|_0 + \lambda \phi_{TV}(u), \tag{1}$$

where $u \in \mathbb{R}^{n\times m}$ is the desired original clean image, $b \in \mathbb{R}^{n\times m}$ is the degraded image, $\lambda > 0$ is the regularization parameter, $o \in \{0,1\}^n$ is specified by the user, $\odot$ denotes an elementwise product, $H \in \mathbb{R}^{n\times n}$ represents a linear operator. Another circumstance, when $H = I$, the identity operator, the problem simplifies to one of noise reduction.

In recent work, the ℓ_0-norm has been employed as a data fidelity criterion for impulse noise elimination. [2] proposed the ℓ_0-norm with an OGSTV and MC penalty model, significantly enhancing image restoration performance, especially under high impulse noise conditions. [14] proposed ℓ_0-OGSTV model effectively diminishes staircasing artifacts and precisely restores images marred by impulse noise. [15] successfully incorporated the ℓ_0-norm data fidelity term into a nonconvex generalized regularization framework, improving the model's ability to preserve sharp image contours while minimizing staircase artifacts. Collectively, these models demonstrate the effectiveness of the ℓ_0-norm in restoring images affected by impulse noise.

1.1. Contributions

To the best of our knowledge, the combination of ℓ_0-norm data fidelity, fractional-order total variation and recursive filtering has not been addressed by any of the existing optimization models. Therefore, this has motivated us to combine them for the restoration of MR images in medical imaging. In this article, we focus on addressing the challenge of restoring MR image in medical imaging that have been degraded by blurred boundaries and residual noise. The model comprises an ℓ_0-norm data fidelity term to restore images from impulse noise, a regularizer of fractional-order total variation (FOTV) to eliminate the staircase effects, and the recursive filtering to improve edge quality significantly. Our method capitalizes on the strengths of the forward-backward total variation to provide superior denoising capabilities, effectively mitigating the staircasing artifacts. Additionally, the recursive filtering technique employed not only refines the texture details within medical images, but also reduces the computational process. We employ the alternate direction multiplier algorithm to solve the subproblems. Finally, we conduct numerical experiments to analyze the effectiveness of our proposed model, and the numerical results show our method is very effective.

1.2. Organization

The rest of this article is organized as follows. In Section 2 introduces fundamental ideas and preliminary information pertinent to the proposed algorithm. In Section 3, we propose a novel framework aimed at eliminating blur and impulse noise and derive an efficient algorithm to solve the corresponding minimization problem. In Section 4, the superiority of the proposed method is proved by numerical experiments. Finally, a conclusion is made in Section 5.

2. Preliminaries

In this section, we briefly review a few key components of the ℓ_0-norm fidelity term, the discrete fractional-order difference, the recursive filtering and the alternating direction method of multipliers framework.

2.1. The ℓ_0 Fidelity Term

Initially, we provide an overview of the essential definitions and characteristics associated with ℓ_0-norm fidelity term. In the expression $\|o \odot (Hu - f)\|_0$, the $o \in \{0,1\}^n$ is specified by the user. Specifically, when $o_i = 0$, it implies the pixel in position i is an outlier, while when $o_i = 1$, it implies the pixel in position i is a potential outlier. For this paper, we set $o_i = \begin{cases} 0, & t_i = u_{min} \text{ or } u_{max} \\ 1, & \text{otherwise} \end{cases}$ for the impulse noise.

The following lemma, as meticulously outlined in the work of [13], elucidates the variational formulation that underpins the ℓ_0-norm.

Lemma 1
For any given $w \in \mathbb{R}^n$, it holds that

$$\begin{aligned} \|w\|_0 = \min_{0 \le z \le 1} & < 1, 1 - z >, \\ s.t.\ & z \odot |w| = 0, \end{aligned} \tag{2}$$

and $z^* = 1 - sign(|w|)$ is the unique optimal solution to problem Eq. (2). Here, the standard signum function sign is employed in component form, and $sign(0) = 0$.

The result of Lemma 1 implies that the ℓ_0-norm minimization problem in (1) is equivalent to

$$\begin{aligned} \min_{0 \le u,z \le 1} & < 1, 1 - z > + \lambda \|\nabla u\|_1 \\ s.t.\ & z \odot |o \odot (Hu - b)| = 0. \end{aligned} \tag{3}$$

If u^* is an overall optimal solution of Eq. (1), then $(u^*, 1 - sign(|Hu^* - b|))$ is overall optimal solution of Eq. (3). In a similar manner, if u^* is a global Ideal solution of Eq. (3), then $(u^*, 1 - sign(|Hu^* - b|))$ is an overall optimal solution of Eq. (1). The ability of ℓ_0-norm has proven to be remarkably effective in restoring images, offering superior performance.

2.2. Fractional-Order Total Variation

Given an image domain $\Omega \subset \mathbb{R}^2$, we discretize it as a rectangular grid $\{(x_i, y_j) : 1 \le i \le M, 1 \le j \le N\}$. Consequently, the image discretized on the Euclidean plane $\mathbb{R}^{M \times N}$, denoted as $u_{i,j} = u(x_i, y_j)$. Let $C_0^\alpha(\Omega)$ with $\alpha > 0$ be the space of α-order continuously differentiable functions defined on Ω with compact support. Based on the GL fractional-order derivatives, the discrete form of the fractional-order gradient $\nabla^\alpha u$ can be evaluated by

$$\nabla^\alpha u = [D_x^\alpha u, D_y^\alpha u], \tag{4}$$

where α is the fractional-order and we set $1 \le \alpha < 2$ in this paper, where the fractional-order derivatives $(D_x^\alpha u),\ (D_y^\alpha u) \in \mathbb{R}^{M \times N}$ along the x-axis and the y-axis are approximated by the

$$\begin{cases} (D_x^\alpha u)_{i,j} = \sum_{k=0}^{K-1} (-1)^k C_k^\alpha u_{i-k,j}, \\ (D_y^\alpha u)_{i,j} = \sum_{k=0}^{K-1} (-1)^k C_k^\alpha u_{i,j-k}. \end{cases} \tag{5}$$

In this context, K denotes the quantity of adjacent pixels employed to calculate the fractional-order derivative for each pixel. The coefficients $\{C_k^\alpha\}_{k=0}^{K-1}$ are given by $C_k^\alpha = \frac{\Gamma(\alpha+1)}{\Gamma(k+1)\Gamma(\alpha+1-k)}$ with the Gamma function $\Gamma(x)$. Hence, the discrete fractional-order TV of u is expressed in terms of

$$\|\nabla^\alpha\|_1 = \sum_{i,j} \left(\left| (D_x^\alpha u)_{i,j} \right| + \left| (D_y^\alpha u)_{i,j} \right| \right), \tag{6}$$

where $(\nabla^\alpha)^* = \overline{(-1)^\alpha} div^\alpha$ is the conjugate operator of the fractional order gradient operator. In the discrete case, the vector $div^\alpha p = (p^{(1)}, p^{(2)}) \in \mathbb{R}^{N\times M} \times \mathbb{R}^{N\times M}$ discrete fractional-order divergence is defined as [6, 17]

$$(div^\alpha p)_{i,j} = (-1)^\alpha \sum_{k=0}^{K-1} (-1)^k C_k^\alpha (p_{i+k,j}^{(1)} + p_{i,j+k}^{(2)}). \tag{7}$$

Observe that the divergence Eq. (7) is the adjoint of the gradient Eq. (4).

2.3. Recursive Filtering

The first-order recursive filtering was initially introduced by [16]. Denoting $I[u]$ and $J[u]$ are the noisy image and the denoising image, respectively. Recursive filtering computes $J[u]$ recursively.

$$J[u] = (1-a)^{d[u]} I[u] + a^{d[u]} J[u-1], \tag{8}$$

where $a \in [0,1]$ is a feedback coefficient, and its implementation in $O(N)$ time is straight forward. Besides the scalar constant $a = exp(-\sqrt{2}/\sigma_s)$ is a user defined parameter controlling the relative emphasis of $I[u]$ and $J[u]$,

$$\begin{aligned} d[u] =& 1 + \frac{\sigma_s}{\sigma_r} |I[u] - I[u-1]| \\ =& 1 + \frac{\sigma_s}{\sigma_r} |\nabla I[u]|, \end{aligned} \tag{9}$$

where σ_s and σ_r represent the spatial and range parameters, respectively. The rapid iteration of the recursion in Eq. (8) is attributed to the pre-computed values from Eq. (9) and the independent computation of $J[u]$ for each row. For gray images, one can sequentially perform Eq. (8) forward and backward in two directions. With color images, it's necessary to iterate through this operational sequence for each color channel.

As d increases, a^d goes to zero, stopping the propagation chain, thus preserving edges. Furthermore, the expanded recursion of Eq. (8) also elucidates this issue

$$J[u] = \sum_{\ell=0}^{n} \left(\prod_{k=0}^{\ell} a^{d[u-k+1]} \right) (1 - a^{d[u-\ell]}) I[u-\ell]. \tag{10}$$

2.4. Alternating Direction Method of Mltipliers

The alternative direction method of multipliers is a computational framework for solving optimization problems, which is to solve the following constrained separable optimization problems

$$\begin{aligned} &\min_{u,w} f(u) + g(w) \\ &s.t.\ Au + Bw = d, \\ &u, w \in \chi_i, i = 1, 2, \end{aligned} \tag{11}$$

where $f(\cdot)$, $g(\cdot) : \chi_i \to \mathbb{R}$ are closed convex functions, A, $B \in \mathbb{R}^{l\times n}$ are linear transforms, $\chi_i \to \mathbb{R}$ are nonempty closed convex sets, and $d \in \mathbb{R}^l$ is a given vector. For problem Eq. (11), we establish the augmented Lagrangian function

$$\mathcal{L}_{\mathcal{A}}(u, w; \mu) = f(u) + g(w) + \mu^T(Au + Bw - d) + \frac{\lambda}{2}||Au + Bw - d||^2, \tag{12}$$

where $\mu \in \mathbb{R}^l$ is the Lagrange multiplier and $\lambda > 0$ is a penalty parameter which controls the linear constraint. The objective is to find the saddle point of $\mathcal{L}_{\mathcal{A}}$ by alternatively minimizing $\mathcal{L}_{\mathcal{A}}$ with respect to u, w and μ. The problem Eq. (11) is addressed by presenting the ADMM algorithm as Algorithm 1.

Algorithm 1 ADMM for minimizing the problem Eq. (11).

Input: penalty parameter $\lambda > 0$, number of iterations.
Initialize: Initial image $u^0 = b$, counter $k = 0$, Lagrange multipliers μ.
output: Restored image u.

1: For $k = 0$, compute u^{k+1}, w^{k+1}, μ^{k+1}
2: $u^{k+1} = \arg\min_u f(u) + \frac{\lambda}{2}||Au + Bw^k - d + \frac{\mu^k}{\lambda}||^2$,
3: $w^{k+1} = \arg\min_w g(w) + \frac{\lambda}{2}||Au^{k+1} + Bw - d + \frac{\mu^k}{\lambda}||^2$,
4: $\mu^{k+1} = \mu^k + \lambda(Au^{k+1} + Bw^{k+1} - d)$,
5: $k = k + 1$,
6: until a stopping criterion is satisfied.

3. The proposed algorithm

In this part, we first introduce the proposed MR image restoration model and the corresponding solution methods. Finally, an ADMM solution framework is provided.

3.1. Model

The proposed MR image restoration model is as follows

$$\min_{0\le u\le 1} \|o \odot (Hu - b)\|_0 + \lambda_1 \|\nabla^\alpha u\|_1 + \lambda_2 \phi(u), \tag{13}$$

where $\nabla^\alpha u$ denotes the fractional-order TV. ϕ denotes the recursive filtering. $\lambda_1 > 0$ and $\lambda_2 > 0$ represent regularization parameters.

3.2. Optimization

Using variable splitting, the problem is rephrased as a constrained optimization problem that follows

$$\begin{aligned} \min_{0<u,v\le 1} & < 1, 1 - v > +\lambda_1||x||_1 + \lambda_2(z) \\ s.t. & Hu - b = y \\ & v \odot |o \odot y| = 0 \\ & \nabla^\alpha u = x, u = z. \end{aligned} \tag{14}$$

The corresponding augmented Lagrangian functional is given by

$$\begin{aligned}\mathcal{L}_{\mathcal{A}}(u,v,x,y,z,\mu_v,\mu_x,\mu_y,\mu_z) =& < 1,1-v > +\lambda_1||x||_1+\lambda_2\phi(z)+ < v\odot o\odot|y|,\mu_v > \\ &+\frac{\beta_v}{2}||v\odot o\odot|y|||^2+ < Hu-b-y,\mu_y > +\frac{\beta_y}{2}||Hu-b-y||^2 \\ &+ < \nabla^\alpha u-x,\mu_x > +\frac{\beta_x}{2}||\nabla^\alpha u-x||^2+ < u-z,\mu_z > +\frac{\beta_z}{2}||u-z||^2,\end{aligned} \tag{15}$$

where variables μ_v, μ_x, μ_y, and μ_z are the Lagrange multipliers associated with the constraints of Eq. (14). $\beta_v, \beta_x, \beta_y$, and $\beta_z > 0$ are the corresponding penalty parameters. We utilize the alternating direction method of multipliers [18] to solve the proposed model Eq. (15). According to the ADMM scheme, we can alternately solve for the following problems.

3.2.1. u - subproblem

The u-subproblem is given by

$$u^{k+1} = \arg\min_u \frac{\beta_y}{2}||Hu-b-y+\frac{\mu_y}{\beta_y}||^2+\frac{\beta_x}{2}||\nabla^\alpha u-x+\frac{\mu_x}{\beta_x}||^2+\frac{\beta_z}{2}||u-z+\frac{\mu_z}{\beta_z}||^2. \tag{16}$$

Based on the first-order optimality conditions, we are tasked with resolving a system of linear equation

$$u(\beta_y H^T H+\beta_x(\nabla^\alpha)^T\nabla^\alpha)+\beta_z) = H^T(\beta_y(b+y)-\mu_y)+(\nabla^\alpha)^T(\beta_x x-\mu_x)+\beta_z(z-\mu), \tag{17}$$

where $\mu = \frac{\mu_z}{\beta_z}$, considering u with periodic boundary constraints. Due to the circulant and circulant blocks (BCCB) structure, matrices $(\nabla^\alpha)^T\nabla^\alpha$ and $H^T H$ can be diagonalized by 2D discrete fast Fourier transforms (FFT). Therefore, solving for u can be efficiently solved using 2D FFT and 2D FFT inverse operations. The process for acquiring the optimal u is outlined as follows

$$u^{k+1} = \mathcal{F}^{-1}\left(\frac{\mathcal{F}(\varkappa)}{\mathcal{F}[\beta_y H^T H+\beta_x(\nabla^\alpha)^T(\nabla^\alpha)+\beta_z]}\right), \tag{18}$$

where $\varkappa = H^T(\beta_y(b+y)-\mu_y)+(\nabla^\alpha)^T(\beta_x x+\mu_x)+\beta_z(z-\mu)$, $\mathcal{F}$ and $\mathcal{F}^{-1}$ represent the Fourier transform and its inverse.

3.2.2. v - subproblem

The v subproblem can be written as

$$v^{k+1} = \arg\min_v \langle 1,1-v\rangle + < v\odot o\odot|y^k|,{\mu_v}^k > +\frac{{\beta_v}^k}{2}||v\odot o\odot|y^k|||^2. \tag{19}$$

The v-subproblem in Eq. (19) is equivalent to

$$v^{k+1} = \arg\min_v \frac{1}{2}\beta_v o\odot y^k\odot y^k\odot v^2+v\left(\mu_v^k\odot o\odot\left|y^k\right|-1\right), \tag{20}$$

therefore, projection method is engaged to find the solution v^{k+1}

$$v^{k+1} = \min\left(1,\max\left(0,-\frac{\mu_v^k\odot o\odot\left|y^k\right|-1}{\beta_v o\odot y^k\odot y^k}\right)\right). \tag{21}$$

This subproblem mentioned is a projection onto a convex set, ensuring that the pixel values of the restored image remain within the range of 0 to 1.

3.2.3. y - subproblem

Solving the y-subproblem involves employing a soft thresholding technique coupled with a shrink operator. The formula is presented as follows

$$y^{k+1} = \arg\min_{y} < v^{k+1} \odot o \odot |y|, {\mu_v}^k > + \frac{\beta_v}{2} ||v^{k+1} \odot o \odot |y|||^2 + < Hu^{k+1} - b - y, {\mu_y}^k > + \frac{\beta_y}{2} ||Hu^{k+1} - b - y||^2, \tag{22}$$

Eq. (22) holds equivalence to Eq. (23)

$$y^{k+1} = \arg\min_{y} \frac{\beta_y}{2} \left\| y - \left(Hu^{k+1} - b + \frac{\mu_y^k}{\beta_y} \right) \right\|^2 + \frac{\beta_v}{2} \left\| v^{k+1} \odot o \odot |y| + \frac{\mu_v^k}{\beta_v} \right\|^2. \tag{23}$$

By expanding Eq. (23) and discarding the constant terms, we can rewrite Eq. (23) as

$$y^{k+1} = \arg\min_{y} \frac{1}{2} \left\| y - \frac{\beta_y (Hu^{k+1} - b + \frac{\mu_y^k}{\beta_y})}{\beta_y + \beta_v (v^{k+1} \odot o)^2} \right\|^2 + \frac{v^{k+1} \odot o \odot \mu_v^k}{\beta_y + \beta_v (v^{k+1} \odot o)^2} \odot |y|. \tag{24}$$

The optimal solution is obtained by employing a four-dimensional shrinkage operator. Upon simplifying Eq. (24), we arrive at the following result

$$y^{k+1} = \text{shrink} \left(\frac{\beta_y (Hu^{k+1} - b + \frac{\mu_y^k}{\beta_y})}{\beta_y + \beta_v (v^{k+1} \odot o)^2}, \frac{v^{k+1} \odot o \odot \mu_v^k}{\beta_y + \beta_v (v^{k+1} \odot o)^2} \right), \tag{25}$$

where $\text{shrink}(\text{s}, \gamma) = \text{sgn}(\text{s}) \odot \max\{\|\text{s}\|_1 - \gamma, 0\}$, and $\text{sgn}(\cdot)$ denotes the signum function.

3.2.4. x - subproblem

Variable x in Eq. (26) isupdated by solving the following problem:

$$x^{k+1} = \arg\min_{x} \frac{\beta_x}{2} \left\| x - \left(\nabla^\alpha u^{k+1} + \frac{\mu_x}{\beta_x} \right) \right\|^2 + \lambda_1 ||x||_1. \tag{26}$$

With the aid of the previously mentioned shrinkage operator, the x-subproblem can be directly tackled.

3.2.5. z - subproblem

The z-subproblem is a recursive filtering issue, with the specific form as follows

$$z^{k+1} = \arg\min_{z} \frac{\beta_z}{2} \|z - (u + \mu)\|^2 + \lambda_2 \phi(z), \tag{27}$$

we define $\vartheta = \sqrt{\frac{\lambda_2}{\beta_z}}$ and $\widetilde{z}^{(k)} = u + \mu$, substitute it into Eq. (27).

$$z^{k+1} = \arg\min_{z} \frac{1}{2\vartheta^2} \left\| z - \widetilde{z}^{(k)} \right\|^2 + \phi(z), \tag{28}$$

where $\widetilde{z}^{(k)}$ donates the 'blurry' image, Eq. (28) minimizes the residue between $\widetilde{z}^{(k)}$ and the 'clean' image z by employing the prior $\phi(z)$.

Expanding on this insight, [19] proposed that the ADMM algorithm can be executed without the prior speciffication of ϕ. Consequently, we may utilize recursive filtering for the resolution of Eq. (28). Denoted by ϕ

$$z^{k+1} = \phi_{\vartheta}\left(\widetilde{z}^{(k)}\right). \tag{29}$$

Finally, the Lagrange multipliers are updated by the following

$$\begin{cases} \mu_x^{k+1} = \mu_x^k + \beta_x(\nabla^\alpha u^{k+1} - x^{k+1}) \\ \mu_y^{k+1} = \mu_y^k + \beta_y(Hu^{k+1} - b - y^{k+1}) \\ \mu^{k+1} = \mu_z^k + \left(u^{k+1} - z^{k+1}\right) \\ \mu_v^{k+1} = \mu_v^k + \beta_v \left(v^{k+1} \odot o \odot \left|y^{k+1}\right|\right). \end{cases} \tag{30}$$

Our method is systematically presented in Algorithm 2.

Algorithm 2 solving the minimization problem Eq. (13).

Input: Regularization parameter $\lambda_2 > 0$, α, penalty parameters $\beta_x, \beta_y, \beta_z, \beta_v > 0$, number of iterations.
Initialize: Initial image $u^0 = b$, counter $k = 0$, Lagrange multipliers μ_x, μ_y, μ, μ_v.
Output: Restored image u.

for $k = 0$ **to** number of iterations **do**
  // Solve the subproblems:
  Compute u^{k+1} according to Eq. (18)
  Compute v^{k+1} according to Eq. (19)
  Compute y^{k+1} according to Eq. (22)
  Compute x^{k+1} according to Eq. (26)
  Compute z^{k+1} according to Eq. (28)
  // Update the Lagrange multipliers:
  Lagrange multipliers according to Eq. (30)
  // Check stopping criterion:
  if $\frac{\left\|u^{k+1}-u^k\right\|_2}{\|u^k\|_2} \leq 1 \times 10^{-4}$ **then**
    break
  end if
end for

Additionally, there are two remarks that are worth noting regarding this algorithm.

Remark 1
When $\alpha = 1$, the fractional-order TV degrades to the conventional TV, then the Eq. (26) reduces to the standard total variation regularization issue. In the experimental section, we provide an in-depth analysis of how the value of α impacts the noise reduction capabilities of our proposed model.

Remark 2
When $\phi(u) = \|u\|_{TV}$ (the total variation norm), then the Eq. (28) is a canonical total variation-based image denoising task [20].

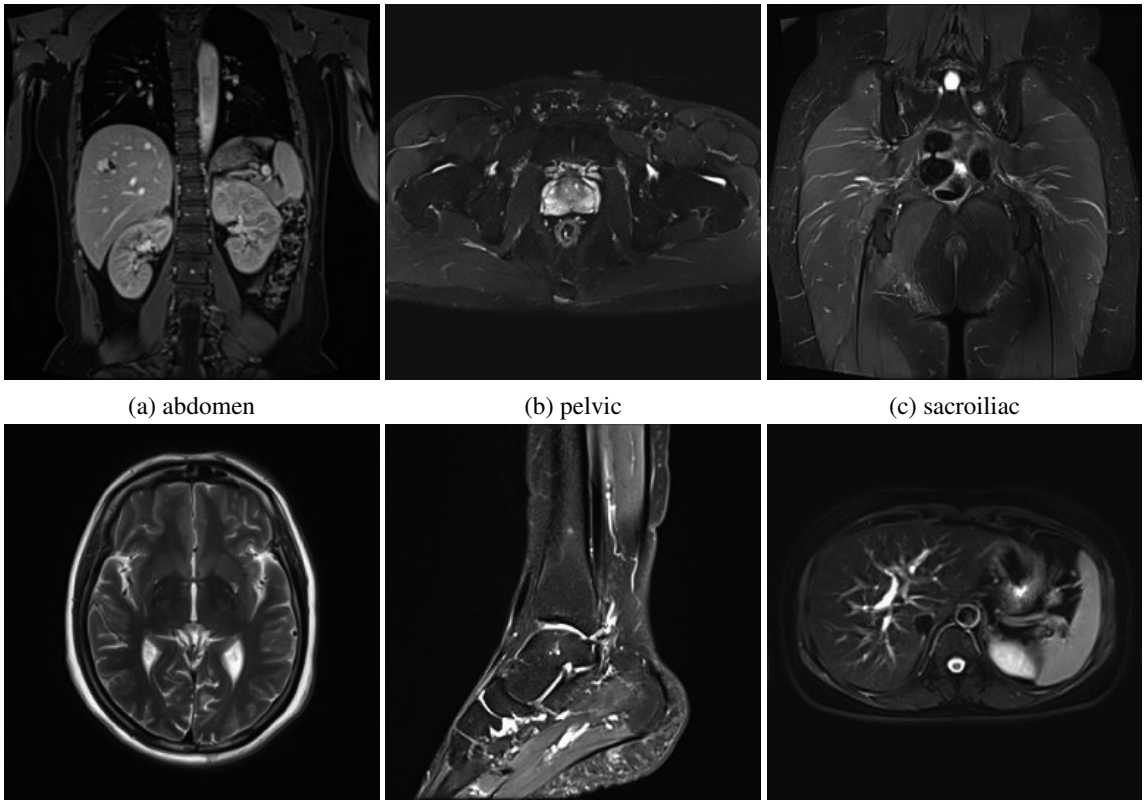

(a) abdomen (b) pelvic (c) sacroiliac

(d) head (e) ankle (f) mrcp

Figure 1. MR images used for the experiments.

4. Numerical Experiments

In this section, we exhibit experimental results that verify the effectiveness of our proposed method for image restoration. The real MR test images are shown in Fig. 1. The experiment is under Windows 10 and MATLAB R2019b operating system, and the CPU is i5-8250U. The restored image quality was assessed through the peak signal-to-noise ratio (PSNR) and the structural similarity index measure (SSIM) [19]. Higher PSNR and SSIM values indicate better image quality.

Our experiments employed a relative error-based stopping criterion for the algorithm.

$$RelError = \frac{\|u_{k+1} - u_k\|}{\|u_k\|} \leq 1 \times 10^{-4}, \tag{31}$$

where u_{k+1} and u_k are the restored image at the current iterate and previous iterate respectively.

4.1. Parameter Selection

The performance of the model is influenced by a number of primary parameters, including the fractional-rder α, the parameters λ_1, λ_2, and penalty parameters of $\beta_v, \beta_x, \beta_y$, and β_z, additionally, these parameters must be meticulously adjusted to achieve higher precision in the outcomes.

Here, we primarily discuss the FOTV term parameter α and the recursive filtering parameter λ_2. Firstly, the value selected for parameter α is crucial importance and the fractional-order α is $1 \leq \alpha < 2$.The parameter λ_1 controls the penalty strength of the FOTV, primarily aimed at mitigating staircase artifacts and enhancing the image restoration

capability of FOTV, which is the main reason we set λ_1 =1 to improve the performance of FOTV. In Fig. 2 the 'head' image was processed with a 5×5 Gaussian blur kernel (σ=5, impulse = 70%) while the 'abdomen' image was subjected to a 7×7 Gaussian blur kernel (σ=10, impulse = 50%). The figures show the PSNR and SSIM values increase with the α value. Therefore, for Gaussian blur, a value of $\alpha = 1.9$ can obtain the best PSNR and SSIM results.

In Fig. 3, the 'ankle' image was processed with a 5×5 average blur kernel (impulse = 70%) while the 'head' image was subjected to a 7×7 average blur kernel (impulse = 50%). Our analysis of the images show that the optimal values for PSNR and SSIM are achieved at $\alpha = 1.3$ value, thus our preference for this value in the context of average blur kernel.

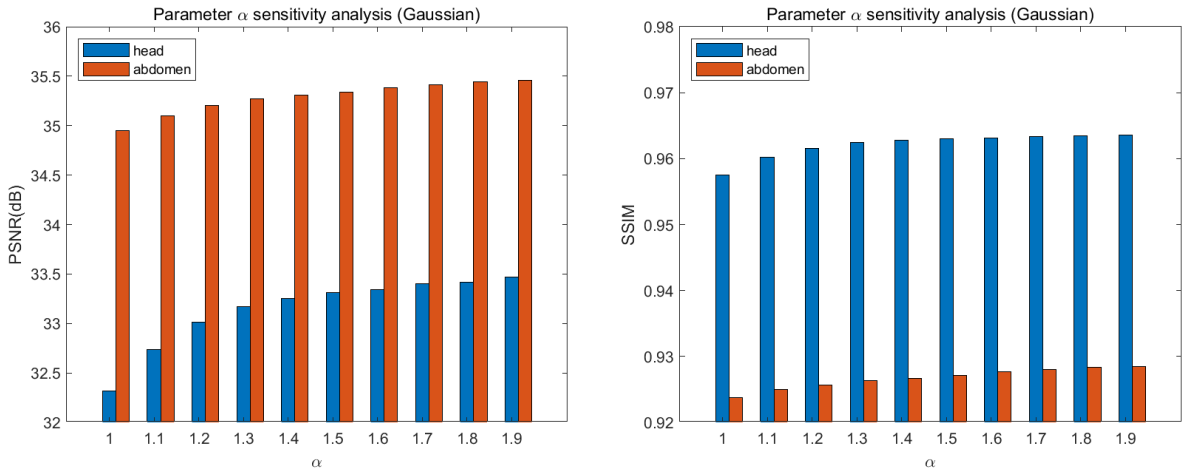

Figure 2. PSNR and SSIM values for images restoration by my method with different α, 'head' (5×5 Gaussian blur kernel, σ = 10 and impulse = 70%) and 'abdomen' (7×7 Gaussian blur kernel, σ=10 and impulse = 50%).

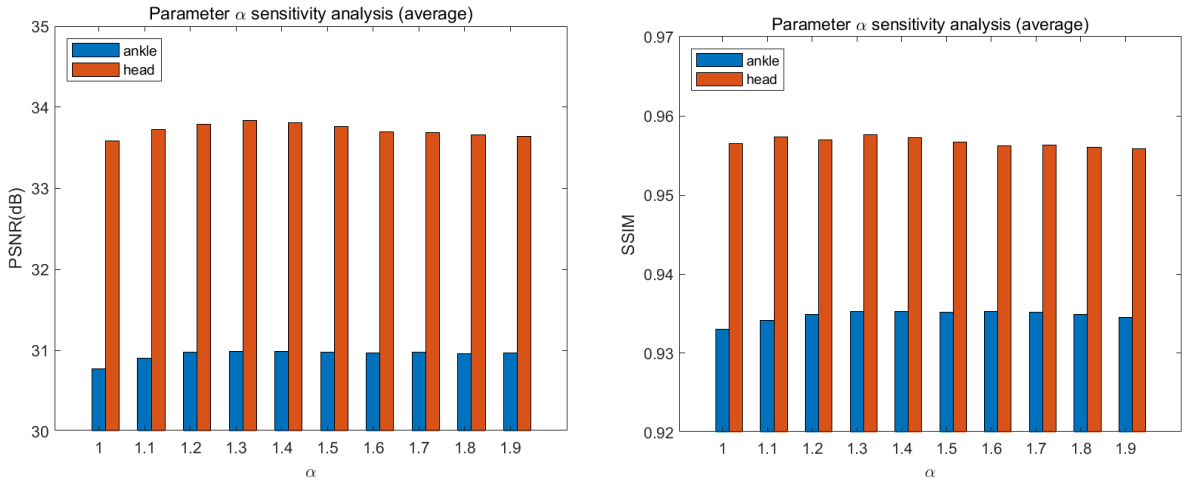

Figure 3. PSNR and SSIM values for images restoration by my method with different α, 'ankle' (5×5 average blur kernel and impulse = 70%) and 'head' (7×7 average blur kernel and impulse = 50%).

In this paper, the parameters λ_2 control the weight and also manage the magnitude of the value ϑ within the recursive filtering. Therefore, the selection of the λ_2 parameter is crucial. In Fig. 4, we conducted experiments with the Gaussian and average blur kernel. The results show that the optimal effect is achieved with $\lambda_2 = 0.001$ when adding a Gaussian blur kernel, and with $\lambda_2 = 0.005$ when adding an average blur kernel.

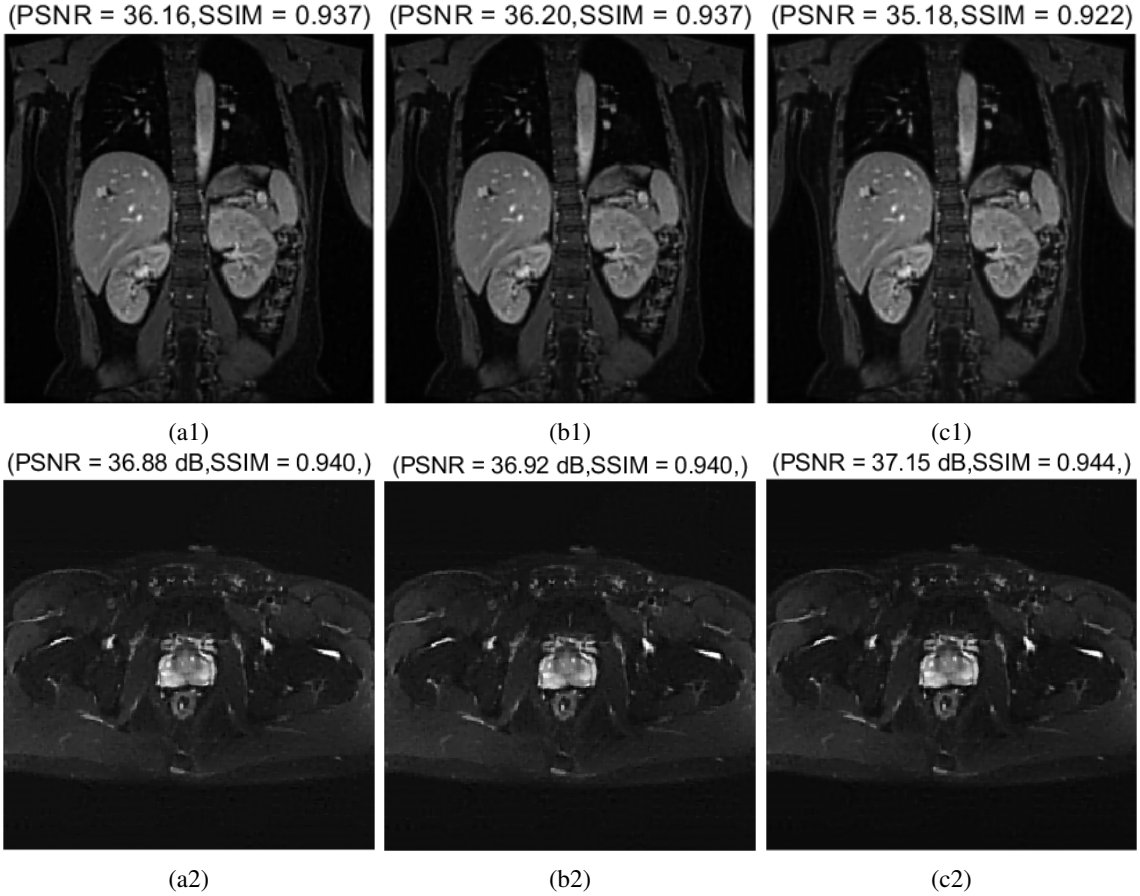

Figure 4. Restoration results of different λ_2 for 'abdomen' (7×7 Gaussian blur kernel, σ=10 and impulse = 30%) and 'pelvic' (7×7 average blur kernel and impulse = 30%).

In this experimental section, this process involves adjusting one parameter at a time while maintaining the remaining parameters at their default values.

4.2. Results and Analysis

The experimental results of our proposed model are compared with three related methods: ℓ_0-OGSTV [14], HNHOTV-OGS [3], and Median Filter (built-in noise reduction technology in MATLAB).

In this experiment, we assumed that the blurring kernel is known. To simulate a noisy blurred image, the original images are processed with a 5×5 Gaussian blur kernel with standard deviation $\sigma = 5$ and a 7×7 Gaussian blur kernel with standard deviation $\sigma = 10$. Additionally, average blur kernels of two distinct sizes, 5×5 and 7×7 are applied to the original images. Subsequently, the blurred images are subjected to impulse noise at varying intensity levels.

For parameters, we fixed $\lambda_1 = 1$. The other parameters were manually selected to obtain the most satisfactory restoration quality. The parameters of HNHOTV-OGS and ℓ_0-OGSTV are consistent with the original text. To assess the performance under varying noise conditions, the test images were subjected to three distinct levels of impulse noise: 30%, 50% and 70% The resulting PSNR and SSIM values, which serve as quantitative measures of restoration efficacy, are presented in Table 1 through Table 4.

In each table, we can observe when using various intensities of noise and different blur kernels, our method almost always achieves higher PSNR and SSIM values compared to the other methods. Only in a few specific cases

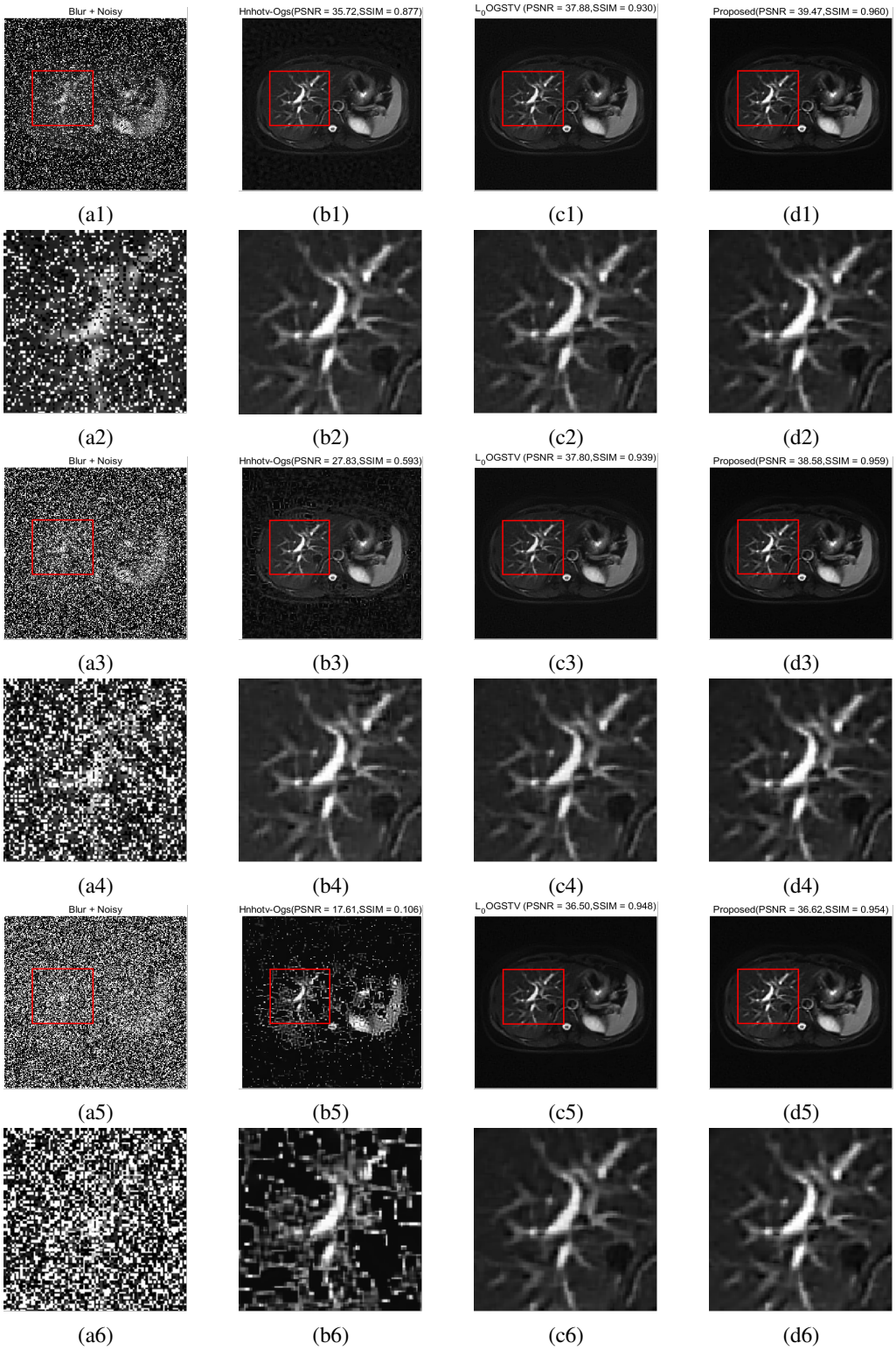

Figure 5. The (1), (3), and (5) rows show the results after applying a 5×5 Gaussian kernel ($\sigma = 5$, impulse = $30\%, 50\%, 70\%$) to the 'mrcp' image. The (2), (4), and (6) rows display the corresponding enlarged image segments. Columns (a1)-(a6) show the noisy versions, (b1)-(b6) are restored with HNHOTV-OGS, (c1)-(c6) with ℓ_0-OGSTV, and (d1)-(d6) with our method.

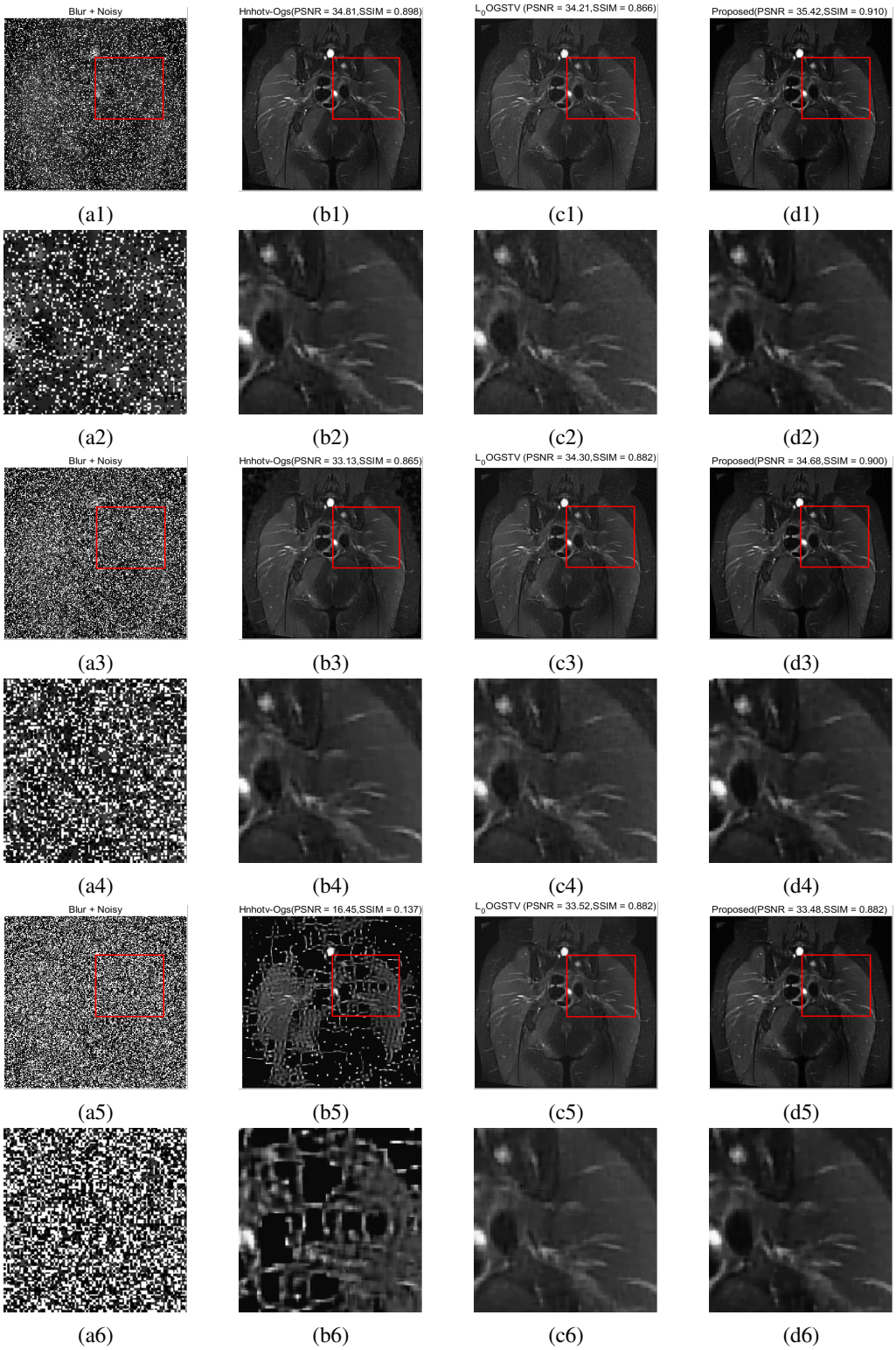

Figure 6. The (1), (3), and (5) rows show the results after applying a 7×7 average blur kernel (impulse = $30\%, 50\%, 70\%$) to the 'sacroiliac' image. The (2), (4), and (6) rows display the corresponding enlarged image segments. Columns (a1)-(a6) show the noisy versions, (b1)-(b6) are restored with HNHOTV-OGS, (c1)-(c6) with ℓ_0-OGSTV, and (d1)-(d6) with our method.

Table 1. Deblurring results for PSNR and SSIM values with 5×5 Gaussian blur kernel (σ=5).

Noise level	Image	Restoration			
		Median_Filter	HNHOTV-OGS	ℓ_0-OGSTV	Proposed
30	abdomen	28.14/0.756	35.69/0.899	37.09/0.939	38.23/0.958
	pelvic	27.52/0.855	37.62/0.938	37.94/0.937	38.81/0.957
	sacroiliac	27.90/0.758	35.86/0.912	36.23/0.912	37.01/0.935
	head	24.14/0.828	34.95/0.904	36.85/0.971	37.18/0.978
	ankle	23.53/0.788	33.30/0.876	35.09/0.956	35.15/0.963
	mrcp	28.62/0.873	35.72/0.877	37.88/0.932	39.47/0.960
50	abdomen	23.70/0.673	29.49/0.735	36.64/0.938	37.26/0.950
	pelvic	23.61/0.770	28.80/0.680	37.48/0.941	37.55/0.953
	sacroiliac	23.94/0.680	30.90/0.803	35.72/0.913	36.07/0.925
	head	21.39/0.744	30.25/0.764	35.68/0.969	35.82/0.974
	ankle	21.35/0.707	28.44/0.670	33.61/0.950	33.65/0.955
	mrcp	23.82/0.786	27.82/0.593	37.80/0.939	38.58/0.959
70	abdomen	13.42/0.288	17.18/0.198	35.21/0.930	35.27/0.932
	pelvic	13.51/0.278	16.14/0.071	35.21/0.940	34.89/0.942
	sacroiliac	13.82/0.245	15.07/0.087	34.27/0.904	34.22/0.902
	head	13.00/0.333	17.00/0.291	33.45/0.962	33.50/0.964
	ankle	13.07/0.297	16.93/0.220	30.69/0.933	30.86/0.935
	mrcp	13.33/0.313	17.24/0.105	36.50/0.948	36.62/0.954

Table 2. Deblurring results for PSNR and SSIM values with 7×7 Gaussian blur kernel (σ=10).

Noise level	Image	Restoration			
		Median_Filter	HNHOTV-OGS	ℓ_0-OGSTV	Proposed
30	abdomen	26.93/0.686	34.98/0.894	35.55/0.917	36.20/0.937
	pelvic	26.70/0.825	36.40/0.932	36.18/0.916	36.82/0.943
	sacroiliac	27.05/0.714	34.74/0.897	34.67/ 0.887	35.12/0.910
	head	22.50/0.765	34.00/0.905	34.98/0.962	35.00/0.967
	ankle	22.49/0.732	32.15/0.880	33.10/0.938	32.82/0.944
	mrcp	27.28/0.835	35.49/0.891	36.15/0.907	37.43/0.944
50	abdomen	23.30/0.616	31.99/0.800	34.92/0.910	35.46/0.928
	pelvic	23.32/0.745	31.11/0.791	35.73/0.921	36.08/0.940
	sacroiliac	23.63/0.642	33.16/0.865	34.18/0.880	34.36/0.899
	head	20.59/0.691	31.46/0.802	34.11/0.957	33.89/0.961
	ankle	20.79/0.660	29.43/0.740	31.91/0.931	31.62/0.935
	mrcp	23.41/0.755	30.77/0.727	35.90/0.914	36.78/0.943
70	abdomen	13.40/0.266	18.67/0.228	34.07/0.904	34.08/0.909
	pelvic	13.50/0.268	17.20/0.086	34.56/0.924	34.46/0.929
	sacroiliac	13.80/0.230	16.60/0.139	33.30/0.876	33.34/0.881
	head	12.93/0.308	19.47/0.355	32.49/0.948	32.01/0.945
	ankle	13.02/0.275	20.02/0.291	30.08/0.917	29.77/0.915
	mrcp	13.31/0.300	19.28/0.141	35.17/0.926	35.43/0.941

Table 3. Deblurring results for PSNR and SSIM values with 5×5 average blur kernel.

Noise level	Image	Restoration			
		Median_Filter	HNHOTV-OGS	ℓ_0-OGSTV	Proposed
30	abdomen	28.30/0.753	35.54/0.897	36.92/0.937	37.31/0.950
	pelvic	28.13/0.854	37.70/0.940	37.90/0.936	38.80/0.956
	sacroiliac	28.18/0.756	35.95/0.913	36.26/0.913	37.07/0.933
	head	24.08/0.825	34.92/0.899	36.89/0.971	37.02/0.977
	ankle	23.70/0.786	33.33/0.873	35.27/0.955	35.32/0.964
	mrcp	28.70/0.871	35.64/0.876	37.81/0.927	39.63/0.964
50	abdomen	23.73/0.671	29.25/0.733	36.70/0.939	36.40/0.942
	pelvic	23.76/0.770	27.93/0.651	37.35/0.941	37.65/0.952
	sacroiliac	24.00/0.678	29.79/0.776	35.94/0.917	36.17/0.925
	head	21.35/0.742	29.89/0.751	35.82/0.969	35.69/0.973
	ankle	21.42/0.705	28.55/0.673	33.56/0.950	33.68/0.955
	mrcp	23.81/0.785	27.29/0.571	37.82/0.939	38.66/0.961
70	abdomen	13.42/0.287	16.94/0.189	35.43/0.932	34.49/0.920
	pelvic	13.52/0.277	15.65/0.061	35.06/0.941	35.34/0.943
	sacroiliac	13.82/0.245	14.83/0.075	34.48/0.906	34.23/0.902
	head	13.00/0.332	17.19/0.295	33.58/0.963	33.25/0.962
	ankle	13.08/0.296	16.81/0.209	30.87/0.935	30.99/0.935
	mrcp	13.33/0.313	17.38/0.101	36.61/0.948	36.74/0.956

Table 4. Deblurring results for PSNR and SSIM values with 7×7 average blur kernel.

Noise level	Image	Restoration			
		Median_Filter	HNHOTV-OGS	ℓ_0-OGSTV	Proposed
30	abdomen	26.89/0.684	34.92/0.892	35.32/0.912	35.53/0.927
	pelvic	26.68/0.824	36.45/ 0.932	36.08/0.913	37.15/0.944
	sacroiliac	27.03/0.712	34.81/ 0.898	34.21/0.866	35.42/0.910
	head	22.45/0.763	34.09/0.906	35.32/0.961	35.00/0.964
	ankle	22.46/0.730	32.26/0.880	33.36/0.937	33.38/0.946
	mrcp	27.24/0.833	35.48/0.892	35.65/0.890	37.77/0.951
50	abdomen	23.29/0.614	32.03/0.801	35.03/0.912	34.76/0.917
	pelvic	23.31/0.744	31.08/0.788	35.93/0.922	36.36/0.941
	sacroiliac	23.62/0.641	33.13/0.865	34.24/0.882	34.68/0.900
	head	20.57/0.689	31.40/0.795	34.24/0.956	33.84/0.958
	ankle	20.77/0.658	29.47/0.737	32.17/0.931	32.17/0.937
	mrcp	23.40/0.754	30.57/0.721	35.89/0.909	37.04/0.948
70	abdomen	13.39/0.266	18.76/0.229	34.21/0.908	33.38/0.921
	pelvic	13.50/0.267	17.09/0.084	34.78/0.925	34.85/0.943
	sacroiliac	13.80/0.230	16.45/0.137	33.43/0.877	34.48/0.883
	head	12.93/0.307	19.64/0.356	32.58/0.947	32.03/0.945
	ankle	13.02/0.274	19.80/0.290	30.23/0.918	30.08/0.917
	mrcp	13.31/0.300	19.16/0.135	35.40/0.927	35.67/0.944

does ℓ_1-OGSTV perform slightly better. From Table 1 to Table 4, it can be observed that our method performs well when relatively low levels of noise. Despite a modest reduction in denoising efficacy compared to ℓ_0-OGSTV under conditions of high-density noise, it continues to deliver superior PSNR and SSIM values.

For the Fig. 5 and Fig. 6, we present the outcomes of three distinct denoising models applied to MR images. The image 'mrcp' is subjected to Gaussian blur (5×5 kernel, standard deviation = 5) and 30%, 50%, and 70% impulse noise. The image 'sacroiliac' is treated with average blur and 30%, 50%, and 70% impulse noise. Upon careful examination of the denoising results depicted in Fig. 5 and Fig. 6, along with the corresponding magnified regions, it can be concluded that the HNHOTV-OGS method exhibits perceptible blocky artifacts at low noise levels. Moreover, under high noise conditions, the method's denoising performance deteriorates significantly, with blocky artifacts becoming particularly pronounced. The main competition for our technique is the ℓ_0-OGSTV model, which effectively eliminates impulse noise and mitigates staircase effects through the application of the ℓ_0-norm. Observing Fig. 5 and Fig. 6 under the condition of 30% impulse noise, it is evident that our method demonstrates superior performance in detail recovery compared to other methods.

Despite the introduction of varying degrees of Gaussian and average blur kernels, our approach consistently outperforms its counterparts, maintaining an advantage in yielding better restoration outcomes. This consistent superiority underscores the robustness and effectiveness of our method in handling images with moderate noise levels, leading to improved visual quality and more accurate preservation of fine details.

To demonstrate the significant superiority of the proposed model in image restoration, we employed the edge preservation index (EPI) to evaluate the performance of HNHOTV-OGS, OGSTV, and our proposed model in terms of detail recovery. Fig. 7 illustrates the restoration outcomes under two distinct blurring conditions: one with a 5×5 Gaussian blur kernel with a standard deviation of 5 and an impulse noise level of 50%, and the other with a 5×5 average blur kernel under the same impulse noise condition. The numerical results clearly indicate that our model outperforms the other two methods across both Gaussian and average blurring scenarios, consistently achieving superior restoration in every trial.

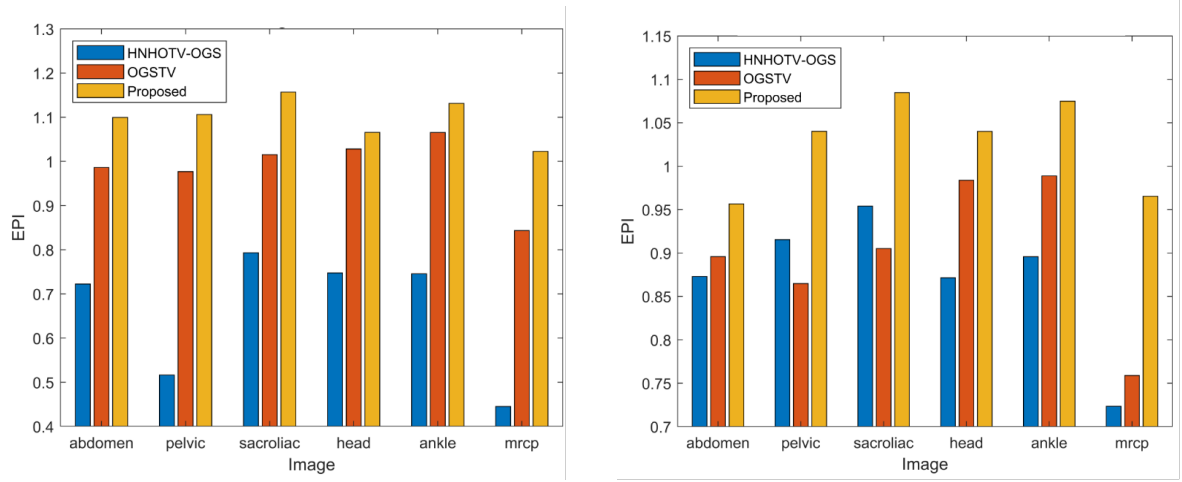

Figure 7. EPI values of HNHOTV-OGS, OGSTV and Proposed restoration results when 5×5 Gaussian blur kernel (σ = 5 and impulse = 50%) and 5×5 average blur kernel (impulse = 50%)

4.3. Verify the Effectiveness of the Method

To verify the effectiveness of our method in eliminating staircasing artifacts using fractional-order regularization, and further reducing noise and enhancing texture through recursive filtering, the following sections will validate these capabilities. Our proposed method is called FOTVF Eq. (13), and the model that removes the third term $\phi(u)$) from FOTVF is named as FOTV. The model is effectively resolved by employing the ADMM algorithm.

Furthermore, the parameters are meticulously aligned with prior uses to ensure continuity and comparability in our analytical framework.

Fig. 8 illustrates the comparative evaluation of the PSNR and SSIM values for the FOTVF and FOTV models at 5×5 Gaussian blur kernel (standard deviation = 5 and impulse = 40%), and Fig. 9 shows the restoration performance for the 'ankle' image, applying the consistent Gaussian blur parameters, including expanded image areas for closer inspection. Fig. 10 illustrates the comparative evaluation of the PSNR and SSIM for the FOTVF and FOTV models at 5×5 average blur kernel (impulse = 60%), and Fig. 11 shows the restoration performance for the 'head' image, applying the consistent average blur parameters, including expanded image areas for closer inspection. The absence of the third term in FOTV causes a substantial drop in both PSNR and SSIM measurements. Furthermore, these figures clearly indicate that the restoration efficacy achieved by the FOTV is less than satisfactory. In contrast, the FOTVF model not only effectively mitigates staircase artifacts but also achieves higher PSNR and SSIM values.

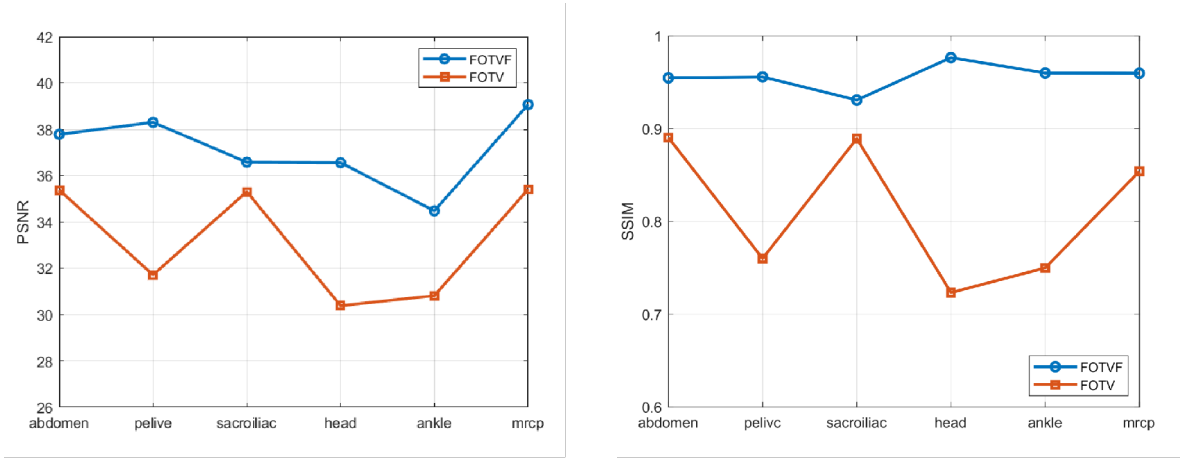

Figure 8. PSNR and SSIM values of FOTVF item and FOTV restoration results when 5×5 Gaussian blur kernel (σ = 5 and impulse = 40%)

5. Conclusion

We proposed a MR image restoration model that combines regularization and filtering methods, aiming at effectively removing impulse noise and staircasing artifacts present in MR images. We demonstrated the effectiveness of using the ℓ_0-norm as a data fidelity term to eliminate impulse noise, while incorporating fractional-order total variation and recursive filtering as penalty terms to mitigate staircasing artifacts and preserve important edges. We solved the proposed model using the alternating direction method of multipliers. In experiments involving Gaussian and average blurring, our method outperformed three other methods in terms of PSNR and SSIM across various levels of blur and noise.

Acknowledgements

This work was supported in part by the Natural Science Foundation of the Anhui Higher Education Institutions of China (No. 2023AH040149), the Anhui Provincial Natural Science Foundation (No. 2208085MF168), and the National Natural Science Foundation of China (No. 12071104).

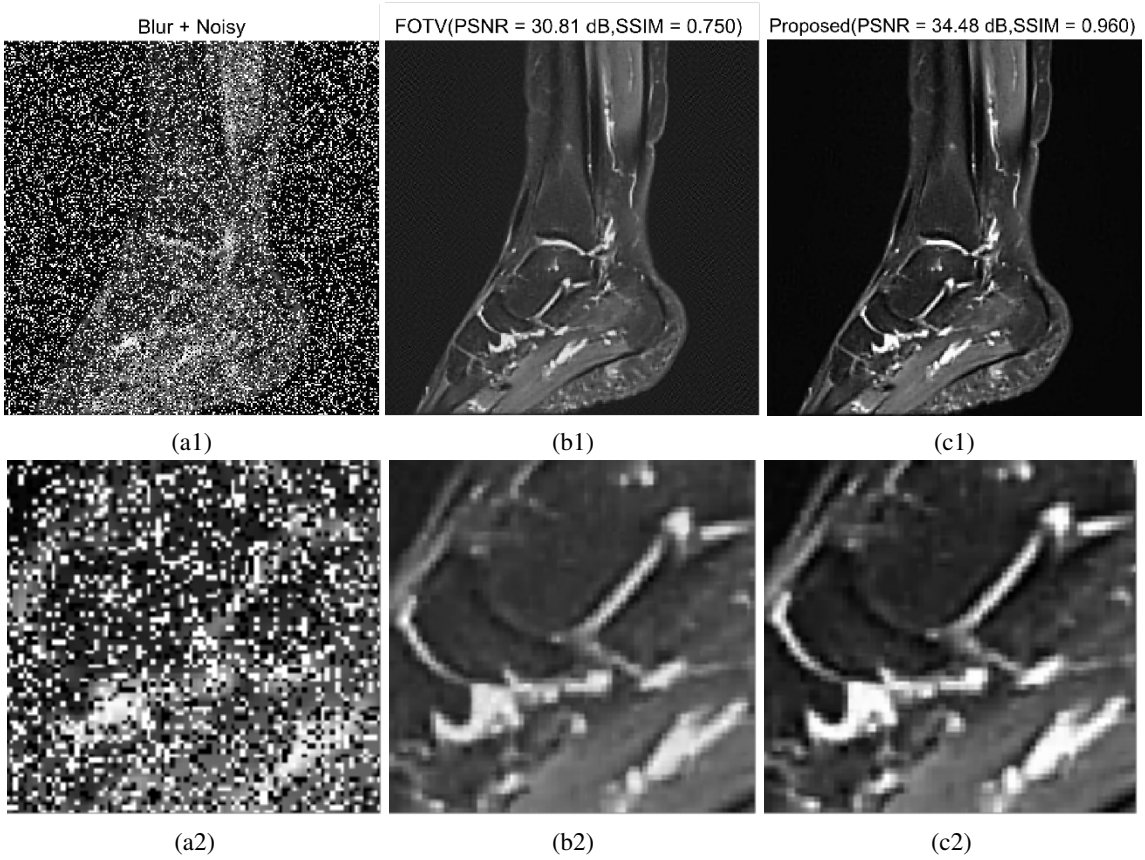

Figure 9. The first line is the recovered results for 'ankle' with 5×5 Gaussian blur kernel ($\sigma = 5$ and impulse = 40%), while the second line shows the fragments corresponding to the zoomed images. (a1)-(a2) blurry image, (b1)-(b2) FOTV restored, (c1)-(c2) FOTVF restored.

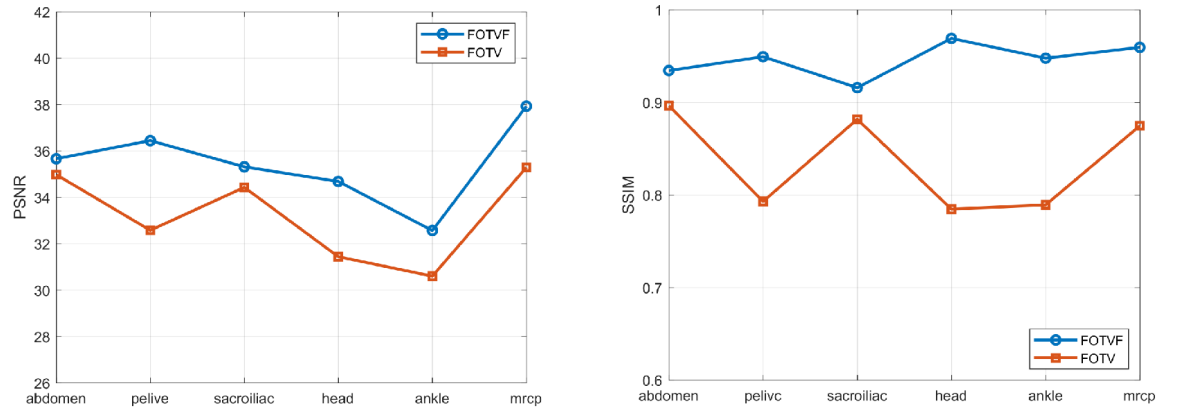

Figure 10. PSNR and SSIM values of FOTVF item and FOTV restoration results when 5×5 average blur kernel (impulse = 60%)

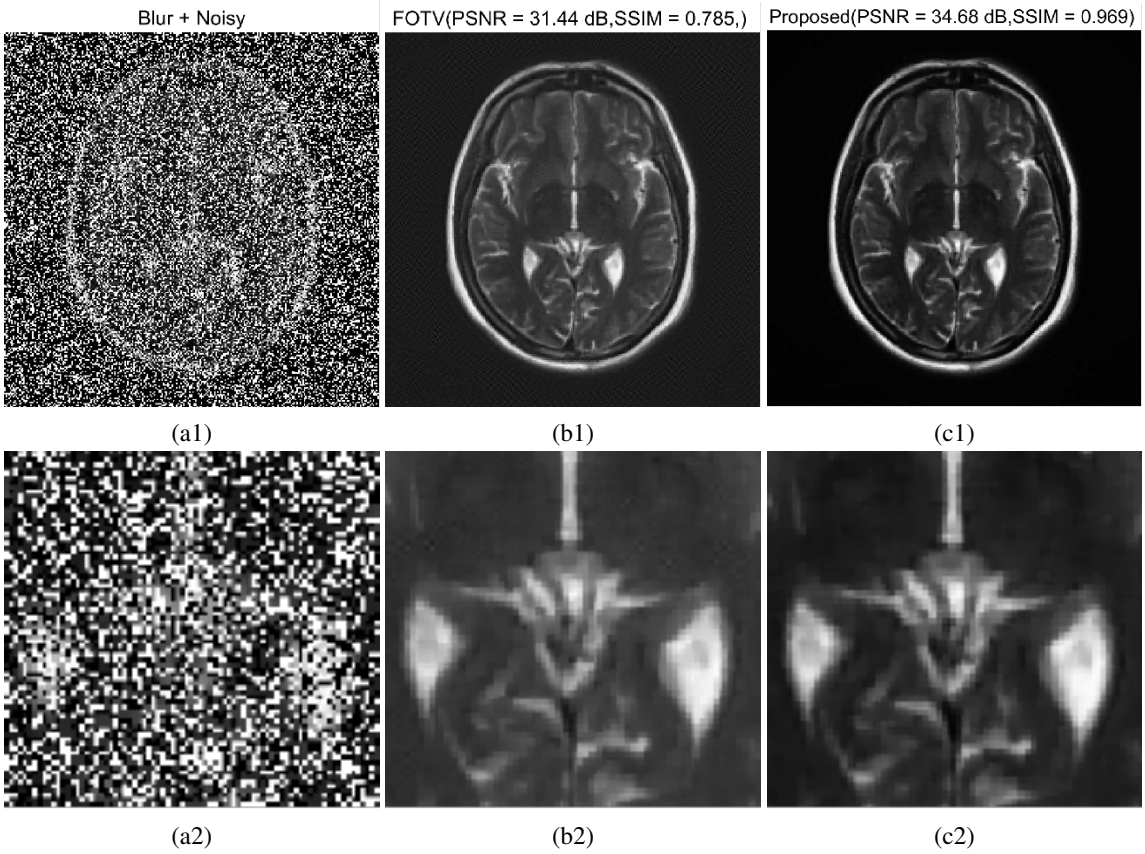

Figure 11. The first line is the recovered results for 'head' with 5×5 average blur kernel (σ = 5 and impulse = 60%), while the second line shows the fragments corresponding to the zoomed images. (a1)-(a2) blurry image, (b1)-(b2) FOTV restored, (c1)-(c2) FOTVF restored.

REFERENCES

1. H. Wei and W. Zheng, *Image denoising based on improved gaussian mixture model*, Scientific Programming, vol. 2021, Article ID 7982645, 2021.
2. W. Xue, Y. Ge, X. Gu, X. Qi, and T. Tao, *Boosting MR image impulse noise removal with overlapping group sparse fractional-order total variation and minimax concave penalty*, Image Analysis and Stereology, vol. 43, no. 1, pp. 53-66, 2024.
3. T. Adam and R. Parameswaran, *Combined higher order non-convex total variation with overlapping group sparsity for impulse noise removal*, Multimedia Tools and Applications, vol. 80, pp. 18503-18530, 2021.
4. X. Liu and W. Lian, *Non-convex high-order TV and ℓ_0-norm wavelet frame-based speckle noise reduction*, IEEE Transactions on Circuits and Systems, vol. 69, no. 12, pp. 5174-5178, 2022.
5. J. Zhu, J. Wei, and B. Hao, *Fast algorithm for box-constrained fractional-order total variation image restoration with impulse noise*, IET Image Processing, vol. 16, pp. 3359-3373, 2022.
6. R. Chowdhury, *Poisson image denoising based on fractional-order total variation*, Inverse Problems and Imaging, vol. 14, no. 1, pp. 77-96, 2020.
7. S. F. Kuang, H. Chao, and Q. Li, *Matrix completion with capped nuclear norm via majorized proximal minimization*, Neurocomputing, vol. 316, pp. 190-201, 2018.
8. H. Zhang, Y. Zhu, and H. Zheng, *NAMF: A nonlocal adaptive mean filter for removal of salt-and-pepper noise*, Mathematical Problems in Engineering, vol. 2021, no. 7, Article ID 4127679, 2021.
9. N. Cao and Y. Liu, *High-noise grayscale image denoising using an improved median filter for the adaptive selection of a threshold*, Applied Sciences, vol. 14, no. 2, Article ID 635, 2024.
10. W. H. Lian and X. W. Liu, *Non-convex fractional-order TV model for impulse noise removal*, Journal of Computational and Applied Mathematics, vol. 417, Article ID 114615, 2023.
11. G. Liu, T. Z. Huang, J. Liu, and X. G. Lv, *Total variation with overlapping group sparsity for image deblurring under impulse noise*, PloS One, vol. 10, no. 4, Article ID e0122562, 2015.

12. J. Lu, Y. Ye, Y. Dong, X. Liu, and Y. Zou, *Impulse noise removal by ℓ_1 weighted nuclear norm minimization*, Journal of Computational Mathematics, vol. 41, pp. 1171-1191, 2023.
13. G. Z. Yuan and B. Ghanem, *ℓ_0-TV: A sparse optimization method for impulse noise image restoration*, IEEE Transactions on Pattern Analysis and Machine Intelligence, vol. 41, no. 2, pp. 352-364, 2017.
14. M. Yin, T. Adam, R. Paramesran, and M. F. Hassan, *An ℓ_0-overlapping group sparse total variation for impulse noise image restoration*, Signal Processing: Image Communication, vol. 102, Article ID 116620 2022.
15. T. Sun and X. W. Liu, *Non-convex TGV regularized ℓ_0-norm fidelity model for impulse noise removal*, Signal Processing, vol. 212, Article ID 109125, 2023.
16. E. S. L. Gastal and M. M. Oliveira, *Domain transform for edge-aware image and video processing*, ACM Transactions on Graphics, vol. 30, no. 4, Article No 69, pp. 1-12, 2011.
17. J. A. Bhutto, A. Khan, and Z. Rahman, *Image restoration with fractional-order total variation regularization and group sparsity*, Mathematics, vol. 11, no. 15, Article ID 3302, 2023.
18. E. Sebastián, M. Franceschelli, A. Gasparri, and E. Montijano, *Accelerated alternating direction method of multipliers gradient tracking for distributed optimization*, IEEE Control Systems Letters, vol. 8, pp. 640-645, 2024.
19. Z. Wang, A. C. Bovik, H. R. Sheikh, and E. P. Simoncelli, *Image quality assessment: from error visibility to structural similarity*, IEEE Transactions on Image Processing, vol. 13, no. 4, pp. 600-612, 2004.
20. S. H. Chan, X. Wang, and O. A. Elgendy, *Plug-and-play ADMM for image restoration: fixed-point convergence and applications*, IEEE Transactions on Computational Imaging, vol. 3, no. 1, pp. 84-98, 2016.
21. A. Shah and J. Bangash, *Comparative analysis of median filter and its variants for removal of impulse noise from gray scale images*, Journal of King Saud University-Computer and Information Sciences, vol. 34, no. 3, pp. 505-519, 2022.
22. N. Cao and Y. Liu, *High-noise grayscale image denoising using an improved median filter for the adaptive selection of a threshold*, Applied Sciences, vol. 14, no. 2, pp. 635, 2024.